Fracture toughness and hardness of transparent MgO-Al2O3-SiO2 glass-ceramics

Leonardo Sant'Ana Gallo, Fabrice Célarié, Jefferson Bettini, Ana Candida M. D. Rodrigues, Tanguy Rouxel, Edgar D. Zanotto

Fracture toughness and hardness of transparent MgO-Al_2O_3-SiO_2 glass-ceramics

Leonardo Sant'Ana Gallo[1*], Fabrice Célarié[2], Jefferson Bettini[3], Ana Candida M. Rodrigues[4], Tanguy Rouxel[2], Edgar D. Zanotto[4]

[1]Departamento de Engenharia (DEG), Universidade Federal de Lavras (UFLA), 37200-900. Lavras, MG, Brazil.

[2]Institut de Physique de Rennes, UMR 6251 UR1-CNRS, University of Rennes 1, campus de Beaulieu, 35042 Rennes cedex, France

[3]Brazilian Nanotechnology National Laboratory (LNNano), Rua Giuseppe Máximo Scolfaro, 10000, Campinas, Brazil

[4]CeRTEV - Center for Research, Technology and Education in Vitreous Materials, Department of Materials Engineering, Federal University of São Carlos, 13565-905 São Carlos, SP, Brazil

*Corresponding author. leonardo.gallo@ufla.br

Keywords: transparent glass-ceramic; high hardness; fracture toughness.

ABSTRACT

Hard and strong transparent glass-ceramics (TGCs) can be used as cooktop plates, telescope mirrors, armor materials, and screens for smartphones and tablets. In this work, transparent glass-ceramics from the MgO-Al_2O_3-SiO_2 (MAS)

system were obtained after a refined heat-treatment protocol. The evolution in fracture toughness, K_{IC} (Single Edge Precracked Beam), and Vickers hardness (H_V) were characterized as a function of the crystallization progress. The K_{IC} of the parent glass was 0.6 MPa.m$^{1/2}$, whereas the TGC samples present values around 1.1 MPa.m$^{1/2}$. The average glass hardness was 8.5 ± 0.8 GPa for loads of 0.6 to 5 N, whereas the H_V of the TGC samples varied from 9 to 10 GPa, for indentation loads ranging from 4.9 to 9.8 N. These results are discussed in light of our previous findings on the evolution of elastic modulus in the same glass-ceramics.

Keywords: Glass-ceramic, glass, crystallization, hardness, toughness

1. INTRODUCTION

Throughout centuries, glass has been used in a wide range of applications, from decoration to medical implants [1], from low tech devices, such as bottles and tableware, to high tech products, such as microscope lenses [2] and optical fibers. Since the accidental discovery of glass-ceramics in 1953 [3], controlled crystallization of glasses has attracted much scientific and technological interest. For example, determining nucleation and crystal growth mechanisms and kinetics is of key interest for developing new-glass-ceramics with improved properties [4]. Also, following the change in physical properties during the crystallization process [5-7] is of the utmost importance to optimize and tailor novel or improved glass-ceramics with improved properties.

Glasses are very brittle materials [8]. However, some applications require improved damage resistance and strength, such as in tablets and smartphone

displays. Glass strengthening can be achieved via ion exchange smaller cations by larger ones on the surface of a material. This process is well-known in industry and is extensively used, e.g., on Gorilla Glass, by Corning (USA) [9], to name probably the most famous product made by this technology. But other leading companies, such as AGC Inc. (JP) and SCHOTT AG (DE), also developed and commercialize similar products. Crystallization also leads to an improvement of mechanical properties, such as hardness [5, 10], fracture toughness [10-13] and elastic moduli [10, 14, 15]. Hardness and fracture toughness are relevant properties and maximizing both simultaneously is challenging. Glass crystallization can result in transparent glass-ceramics (TGC) if at least one situation occurs: i) the glass-ceramic body has a crystal density in the order of 10^{20} crystals.m^{-3} or more [16], which leads to a nanometer crystal size, or ii) the crystallized phase and the residual glass in the glass-ceramic have very similar refractive indexes [17].

In the present article, a transparent glass-ceramic from the MgO-Al_2O_3-SiO_2 (MAS) system was obtained through double-stage crystallization. All the samples underwent the same nucleation heat treatment for the same time at the same temperature. The subsequent crystal growth treatment was carried out at a higher temperature for different periods of time. These treatments were intended to develop the same number of nuclei in all TGCs, thus resulting in the same number of crystals, but with a different mean crystal size. Moreover, since the crystal size should vary with the duration of the final growth heat treatment, the resulting glass-ceramics would likely present different crystallized volume fractions. However, for non-stoichiometric compositions, as in this case, the crystallized volume fraction only increases until or before the coarsening or

Ostwald ripening stage takes over. Therefore, the volume fraction crystallized may be constant for several of these treatments. In a previous work [14], the evolution of the crystal phases with temperature and time, as well as the change of Young modulus during crystallization, were described for the same glass composition, using samples of the same batch as those used here. The current research intends to unveil and describe the evolution of hardness (H_V) and fracture toughness (K_{Ic}) as a function of the crystallization progress. We also observed that the crack propagation resistance estimated by means of the indentation cracking technique (ICT), is in poor agreement with the actual K_{IC}, as measured with the self-consistent SEPB method. In fact, although ICT is frequently called fracture toughness, this technique only provides an estimate of the indentation cracking resistance, as pointed out in previous publications [18,19].

2. EXPERIMENTAL

2.1. GLASS SYNTHESIS AND CHARACTERIZATION

The composition of the investigated glass is presented in Table 1. This composition was developed in our former study [14] and the analyzed samples are of the same batch.

The concentration of nucleating agents (TiO_2 and ZrO_2) was chosen after a study by Fokin and Zanotto [20], which shows that bulk nucleation in a cordierite glass of this same chemical system occurs when a minimum of ~7 mol % of TiO_2 is added. Lower amounts only resulted in surface nucleation, which is not desired for tailoring glass-ceramics.

Al_2O_3 (purity > 98%), SiO_2 (> 99%), B_2O_3 (> 98%), TiO_2 (> 98%) and Sb_2O_3 (> 98%) and MgO (> 98%) and ZrO_2 (> 99%) were used as the starting chemicals. The glass was obtained by the classical melt-quenching method, with a melting temperature of 1520 ºC for 3 hours, during which, the glass was quench and crushed to improve homogeneity. After melting, an annealing treatment was carried out at 735 ºC for 1 hour. Differential scanning calorimetry (DSC) analyses were conducted using a thermal analysis equipment (NETZSCH DSC 404) on both the powdered and bulk samples at a heating rate of 10 K/min from room temperature to 1200 ºC. High temperature X-ray diffraction (HTXRD) was conducted for the bulk samples by a D8 X-ray diffractometer (Bruker AXS), and monochromatic Cu-$K\alpha_1$ radiation using an incident beam Ge monochromator, a Lynx Eye detector and a HTK1200 heating chamber (Anton Parr). The data was recorded over the 10-80° 2θ angular range, with a step of 0.02° and an acquisition time of 0.5s per step. The results were previously published, and further details may be found in [14].

2.2. HEAT TREATMENT PROTOCOL

As mentioned above, glass samples were submitted to a heat-treatment protocol aiming to obtain the same crystal number density and different crystal sizes, which in turn leads to different crystallized volume fraction. This heat treatment protocol was the same used in our previous study [14], in which the *in-situ* evolution of Young's Modulus (E) was investigated during the crystallization process. All samples were nucleated at the same temperature for the same time, i.e., at 733 ºC for 48 hrs. The crystal growth treatment was performed at 900 ºC, for different periods: 31 min; 61 min; 92 min and 153 min. This heat treatment

protocol was chosen, because after a series of heat treatment attempts followed by hardness measurements, it led to the highest hardness values. Each of these heat-treatment durations represent different moments of the evolution of E *versus* time [14] from the beginning of crystal growth (31 min) to the point where no change in the Young Modulus was observed (153 min). Crystallization heat treatment was conducted in a Nabertherm furnace model L3/12/P320. Concerning the crystal phases present, as shown in [14], the first crystalline phase formed was karooite ($MgTi_2O_5$), which was detected during the nucleation stage at 733 ºC for two days. After 31 minutes of the subsequent heat treatment at 900 ºC, four other crystalline phases were identified: spinel ($MgO.Al_2O_3$), rutile (TiO_2), sillimanite ($Al_2O_3.SiO_2$), and sapphirine ($4MgO.5Al_2O_3.2SiO_2$).

2.3. HARDNESS, INDENTATION CRACK RESISTANCE (K_C), AND FRACTURE THOUGHNESS (K_{IC}) MEASUREMENTS

Samples for Vickers hardness tests had parallel surfaces with one mirror polished surface and were at least 5 mm thick. Vickers hardness experiments on glasses were conducted with a Fischerscope HC100 instrumented indenter using 0.6 and 1 N (100 grf) loads. The dwell time at peak loads was set at 5 s. For higher applied loads, i.e., from 4.9 to 196.1 N, a Matsuzawa microindenter (Model VMT-7s, Akita, Japan) was used on glass and on glass-ceramics samples with a dwell time at peak loads of 15 s. Vickers' hardness (Hv) was calculated according to Meyer's expression $Hv = P/(2a^2)$ (1); where P (in Newtons) is the peak load applied on the indenter and a (in meters) is half the diagonal of the projected indentation print. Five indents for each load were performed, except for the load of 196.1 N, due to severe damage to the sample.

Micrographs and crack size and impression diagonal measurements were conducted using the cell[A] software, from Olympus BioSystems GmbH. Experimental errors are related to the image resolution and the operator's skills to perform measurements.

Indentation fracture toughness was calculated according to the equation proposed by Anstis et al. [21]:

$$K_C = 0.016\left(\frac{E}{H_0}\right)^{1/2}\frac{P}{c^{3/2}} \quad (2)$$

where *E* is the elastic modulus, H_0 (=Hv) is hardness, *P* is the load (N) and c is *l*+a (*l* is the crack length and *a* is the half diagonal of the indentation). Samples for fracture toughness tests had four sides polished and one of them mirror finished. The sample size was 5x5x20 mm^3.

All measurements were conducted in ambient atmosphere, with an average humidity of 38 % for tests performed with the Fischerscope HC100 indenter and average humidity of 42% for tests conducted with the Matsuzawa microindenter.

2.4. K_{IC} MEASUREMENTS

Fracture toughness (K_{IC}) measurements were conducted in glasses and glass-ceramic samples using the Single Edge Pre-cracked Beam (SEPB) method with a 20 mm-span 3-point bending support (see ref. [23] for further details). A series of aligned Vickers indentations, spacing 250 µm each, were performed using a Matsuzawa microindenter apparatus, applying a load of 9.81 N. A pre-crack formed from the imprints after applying a compressive load (using a Lloyd LR 30K universal testing machine) by means of the bridge indentation technique, as shown in Figure 1.

Then, the samples were submitted to a 3-point bending test using an Instron 1380 universal testing machine. This equipment was specially designed to achieve a displacement measurement with high resolution and high precision in the specimen deflection measurement, combined with small machine compliance. Fracture toughness was calculated according to equation 3 [24]:

$$K_{IC} = \frac{P_f S}{B W^{1.5}} f\left(\frac{z}{W}\right) \tag{3a}$$

$$f\left(\frac{z}{W}\right) = \frac{3\left(\frac{z}{W}\right)^{1/2}\left[1.99 - \left(\frac{z}{W}\right)\left(1 - \left(\frac{z}{W}\right)\right)\left(2.15 - 3.93\left(\frac{z}{W}\right) + 2.7\left(\frac{z^2}{W^2}\right)\right)\right]}{2\left(1 + 2\left(\frac{z}{W}\right)\left(1 - \left(\frac{z}{W}\right)\right)^{3/2}\right)} \tag{3b}$$

were P_f is the maximum fracture load, S is the support span, B is the specimen thickness, z is the size of the pre-crack, and W is the specimen width. The equation above is valid for the case where the support span length is four times larger than the specimen's thickness.

2.5. MICROSTRUCTURE ANALYSIS

Transmission electron microscopy (TEM) analyses were conducted using a TEM-FEG JEM 2100F microscope, Jeol, Japan. Sample preparation for the TEM analyses consists of hand milling the glass-ceramics, mixing it with alcohol and letting the solution rest for 10 min. The supernatant of this solution was dropped on a 300 mesh Cu grid and placed in a plasma cleaner for the analysis. In addition to the microstructure view, Energy Dispersive X-Ray Spectroscopy (EDS) analysis was conducted to observe the chemical element distribution in glass-ceramic samples. This analysis helps us understand how crystallization occurs.

3. RESULTS AND DISCUSSION

3.1. DSC ANALYSIS AND HEAT TREATMENTS

Figure 2 shows the DSC traces of small monolithic and powder samples of the studied glass composition. The coincidence of the curves is indicative of internal nucleation, which is a necessary condition to obtain glass-ceramics. The DSC trace presents three crystallization peaks up to 1250 ºC. The glass transition temperature (Tg) is an inflection, in the endothermic direction and was estimated via the tangent method, as shown in Figure 2. For the studied glass, Tg ~ 733 ºC, and the crystallization peak maxima are located at 916 ºC, 1011 ºC, and 1168 ºC. In the chosen heat treatment, the nucleation step was carried out at Tg, whereas crystal growth was performed at 897 ºC, which is lower than the temperature of the first DSC crystallization peak. As mentioned in section 2.2, this heat treatment protocol was chosen after several attempts, guided by hardness measurements, to reveal which one leads to a material with highest hardness. The objective was to obtain hard transparent glass-ceramics with various crystalline fractions.

3.2. HARDNESS AND INDENTATION FRACTURE TOUGHNESS

3.2.1. GLASS

Figure 3 presents images of Vickers imprints performed on glass samples, for different applied loads.

With increasing loads, the size of the imprints and the damage on the samples increases. Up to 4.9 N, no cracks were visible to the naked eyes. Median cracks occur at 9.8 N, and lateral cracks also appeared at larger loads. Figure 4 shows the estimated average hardness as a function of the applied load.

The dependence of Hv observed for loads below 10 N is known as the indentation size effect (ISE) and is common for brittle materials investigated by means of the Vickers indentation method. The ISE effect can be attributed to a competition between the indentation volume (scaling with a^3) and the area of contact (scaling with a^2) [25]. This behavior at low loads is closely linked to the plastic energy dissipation mechanisms taking place during an indentation test, and is commonly observed for glasses such as borosilicate, aluminosilicate, soda lime silica, and fused silica [26]. In the present work, Hv tends to decrease with an increasing applied load, from 600 mN to 9.8 N. Then, for the applied load of 49.03 N, a small increase is observed, but still within the experimental error. A significant change in behavior is observed when a load of 98.07 N is applied. At this load, Hv seems to increase and becomes constant if the load is further increased. This is because a significant fraction of the mechanical work is dissipated through the formation of cracks, so that less energy is available to form the imprint. Hence, the larger the crack surface area is (especially stemming from lateral cracking) and the less reliable the value for Hv becomes. This behavior is shown for indentations carried out at 98.07 and 196.1 N. It is important to point out that the presence of small lateral cracks, such as the ones observed under loads of 9.8N and 49.03 N, does not invalidate the measurement. Moreover, the smaller size of the imprints originated by 98.07 N, as compared to the imprint originated by 110 N, leads to an overestimated mean hardness value. Thus, the most reliable average value of H_v for the present glass is 8.5 ± 0.8 GPa, taken at 49 N, which is outside the ISE effect zone and extensive cracking zone. This hardness is relatively high in comparison to most oxide glasses, with hardness around 6 GPa. In fact, this

glass composition was chosen to obtain, after crystallization, suitable glass-ceramics for ballistic armor applications [26].

3.2.2. GLASS-CERAMICS

The evolution of Hv with crystallization was followed for the different heat-treatments applied to the precursor glass. Following a previous report dealing with the effect of the thermal cycle on the microstructure and Young modulus [14], the crystallized glass-ceramics were subjected to the same nucleation treatment (48 h at 733 ºC), but different crystal growth soaking times at 900 ºC: 31, 61, 92 and 153 minutes. E varies considerably in the early stages of crystallization at 900 ºC [14]. The evolution of K_{IC} and H_V during the same crystallization stage is discussed below.

Hardness and indentation cracking were investigated, as a function of time, using the same loads: 4.9 N; 9.8 N; 49.03 N; 98.07 N; 196.1 N. Figure 5 presents the imprint profiles in each sample for each load and Figure 6 presents the calculated hardness of the glass-ceramics.

By comparing the imprint profiles of the glass and the glass-ceramics (Figures 3 and 5, respectively), the indentation damage resistance increases in the glass-ceramics. In fact, for the same applied load, the imprint is larger for the glass than for the glass-ceramic. Although radial cracks generally show up at lower loads than lateral cracks [18], in the case of the glassy samples, these two types of cracks were found to appear almost concomitantly and for the same load of 9.8 N. In contrast, radial cracks appear at 4.9 N in TGCs while lateral cracks show up at 49.03 N (optical observation). A tentative explanation is that glasses, being less compact due to the free volume content, they can partially adapt to the sharp

contact loading by means of a densification process, so that cracks show up at larger loads. In the case of TGCs, their atomic structure is more compact, in average, so that there is less room for densification and cracks tend to appear at smaller loads.

The lower crystalline fraction (roughly estimated to be 30 %, from TEM images, Section 3.4) of samples after nucleation treatment only may explain why the behavior is quite close to that of the parent glass, with extensive cracking occurring at 98.07 N and at larger loads (Figure 5). This explains the scattered hardness values and the (apparently) larger Hv, as seen in Figure 6b) for 98.07 N.

The different crystalline fractions and phases present in each glass-ceramic might explain their distinct hardness observed for different loads. In fact, high-temperature X-Ray diffraction (HT-XRD) showed that after 48 h at 733 ºC, followed by 31 min at 900 ºC, four crystalline phases appeared in the following order: karooite ($MgO.2TiO_2$), spinel ($MgO.Al_2O_3$), rutile (TiO_2) and sillimanite ($Al_2O_3.SiO_2$). In addition, samples subjected to longer soaking times at 900 ºC also presented sapphirine ($4MgO.5Al_2O_3.2SiO_2$) [14]. It is important to point out that, although the glass composition is based on the cordierite composition ($2MgO.2Al_2O_3.5SiO_2$), cordierite crystalline phase was formed when samples from this base-glass were heat treated at temperatures higher than 1,200 ºC, but such heat treatments did not present lead to transparent glass-ceramic samples due to excessive crystal growth. For all samples, including the parent glass, hardness values derived at indentation loads larger than 49.03 N are biased since a significant fraction of mechanical work is dissipated through the creation of

cracks at the indentation sites, leading to smaller imprints, and thus to overestimated Hv values.

Each of these glass-ceramic samples represents different crystallization stages, with increasing values of E and shear modulus (G) [14] as the crystallization at 900 ºC proceeds. However, this Hv does not exhibit the same monotonic trend in glass and TGC as different cracks and densification due to crystallization occur in the TGCs.

3.3. K_{IC} MEASUREMENTS

A typical fracture surface after the three-point bending fracture stage of the SEPB method is shown in Figure 7. The pre-crack (bottom) is clearly distinguished from the fast-propagating crack region. The imprints and the generated cracks are seen at the bottom of the sample. The estimated values of K_{IC} are shown in Figure 8. For the sake of comparison, the values derived from the ICT method and calculated using the Anstis equation [20] is added.

All glass-ceramics exhibit the same fracture toughness values (within the error limits) 1.1 ± 0.1 MPa.m$^{1/2}$; a value that is approximately 90 % larger than for the glass (0.58 ± 0.03 MPa.m$^{1/2}$). Results obtained with the indentation crack length technique are much smaller [18]. The suitability of indentation cracking methods to estimate the fracture toughness of glass and glass-based brittle materials was already questioned [18]. Barriers for crack propagation cause crack deflection and bowing, thus enhancing the fracture toughness of different materials, since energy is consumed to brake or to surround the second-phase particle [27]. Overall, the K_{IC} increased from 0.58 MPa.m$^{1/2}$ for the glassy sample to 1.1 MPa.m$^{1/2}$ for the glass-ceramic, which indicates that the nanometric crystals

indeed impose a barrier to crack propagation, but this barrier does not increase with the crystallized volume fraction observed in this study. The fracture toughness of the different crystalline phases, if taken separately, should differ considerably from each other, as well as from the residual glass. Glasses tend to have low K_{IC} since they do not have a microstructure that presents a barrier to crack propagation. As crystal phases grow, KIC values increases, as shown in [12]. However, the nanometric size of the crystals, relatively small volume fraction, and the fact that all crystal phases are well dispersed masks the effect of different K_{IC} of each phase present. Unfortunately, nanocrystals are much less effective to toughen a material than microcrystals. That is why no significant difference in K_{IC} was observed amongst the various nano glass-ceramic samples. As it can be seen in the TEM images in section 3.4 below, the microstructure difference between TGCs is small.

3.4. MICROSTRUCTURE ANALYSIS

The microstructure of the glass-ceramic samples was analyzed by transmission electron microscopy. All the GCs obtained were transparent. Thus, it is expected that the crystals were smaller than 380 nm, which was confirmed by TEM analysis, shown in figure 9. The images were obtained in scanning mode; the STEM images of each sample are presented below in both bright and dark field modes.

It also shows that all samples presented a high number of nuclei. The amount of the residual glass decreases with time at 900 ºC, as expected. It is not possible to distinguish each crystalline phase among the observed crystals, which are only 20-50 nm. Microstructure plays an important role in toughening glass-ceramics,

and although the GCs presented an increase of ~90% in K_{IC} values compared to the glass, there is seemingly little dependence on the thermal treatment duration, i.e., on the state of progress of the crystallization process. This can be explained by the nanometric size of the crystals. Crystallization has a significant influence on K_{IC}. Nevertheless, crack deflection, bowing, branching or bridging effects are unlikely to be very efficient in the present case due to the nanometric size of crystals. At this stage of our understanding, the toughness improvement probably stems from the composition change of the residual glassy phase, in conjunction with an increase of the material stiffness and a tortuous crack path, in-between the small crystals.

An element mapping was also performed in STEM mode combined with an energy dispersive X-ray detector (STEM-EDS). We remind here, that, in accordance with previous studies [14], the first phase to appear was karooite ($MgO.2TiO_2$), which was detected during the nucleation stage at 733 ºC for 2 days. After 31 minutes of the subsequent heat treatment at 900 ºC, four crystalline phases were identified: spinel ($MgO.Al_2O_3$), rutile (TiO_2), sillimanite ($Al_2O_3.SiO_2$), and sapphirine ($4MgO.5Al_2O_3.2SiO_2$). For this reason, the elements Mg, Ti and Al were analyzed by EDS mappings. Antimony and zirconium were not analyzed as they were not found in any detected crystal phase. Since SiO_2 is the most abundant oxide, the distribution of Si is expected to be widely spread and will not provide valuable information, therefore it is not presented here. Figure 10 shows the distribution of Mg in the TGCs.

The EDS measurements show that Mg is widely spread in the TGC sample obtained with the lowest growth time (31 min at 900 ºC). Nonetheless, the mapping was expected to show more concentrated regions than it really shows

as Mg is present in 2 out of 4 crystal phases observed at this time and temperature, i.e., karooite ($MgO.2TiO_2$) and spinel ($MgO.Al_2O_3$) [14]. As the time at 900 ºC increases, regions of high density (brighter color) show up in the EDS, corresponding to the increase of the crystal phases contents containing that element. After 61 min at 900 ºC, Mg is now present in 3 out of the 5 crystal phases detected. As time at 900 ºC increases, the distribution of Mg in the TGC samples becomes uniform, indicating that the crystal phases containing this element spread all over the sample.

Figure 11 presents the evolution of Ti distribution in TGC crystals.

An agglomeration of titanium can be observed from the early stages of crystal growth. Ti is the main nucleating agent and is present in two out of the four crystal phases found in this TGC after 31 min of growth at 900 ºC. One of the phases is pure TiO_2, and the other is magnesium titanate. After 92 min at 900 ºC, the high concentration zones of Ti and Mg are equivalent, leading to the conclusion that the amount of $MgO.2TiO_2$ has increased. This crystal phase may be used by sapphirine as a substrate to its nucleation.

The EDS shows an agglomeration of Al starting in the early stages of crystal growth. In fact, Al is present in three detected phases: spinel ($MgO.Al_2O_3$), sillimanite ($Al_2O_3.SiO_2$), and sapphirine ($4MgO.5Al_2O_3.2SiO_2$). At longer times of crystal growth at 900 ºC, the Al distribution becomes uniform, which means that the crystal phases containing that element are now widely spread throughout the sample.

The analysis of Figs. 9 – 12 show that the crystals have a mean size of less than 50 nm. The evolution of the Ti ion distribution emphasizes its role as a nucleating agent. In fact, it is possible to observe Ti concentration in certain regions from the

early stages of the crystal growth treatment. This observation supports the idea that a Ti-rich phase nucleates, grows, and works as a substrate for crystallizing further crystal phases.

Important observations can be made regarding the microstructure and the analyzed mechanical properties, hardness, and fracture toughness. Concerning hardness, as crystallization progresses, i.e., as the growth time at 900 ºC increases, the number of crystals increases. The TGC samples are harder than the parent glass, as expected. Nevertheless, H_v change very little as the time of crystal growth increases. Since crystals are harder and stiffer than the glass, mechanical properties reflecting bulk changes, such as hardness or stiffness (see e.g. ref. [14]), increase upon the crystallization process, consistently with the results shown in Fig. 6b. A significant increase of K_{IC} is observed as soon as crystallization occurs. However, no further improvement is noticed as the duration of the thermal treatment is increased. A possible explanation is that the crystal size does not significant changes during the crystallization process, due to the high density of nuclei, as seen in Figs. 9 – 12.

A change was expected in the mechanical properties with the number of crystals or their size [28], i.e., with increasing crystallized fraction. However, it is interesting to note that K_{Ic} remains almost constant as a function of heat treatment time, probably because the crystallized volume fraction does not vary significantly. Also, the occurrence of residual stresses due to the mismatched properties between the residual glass and the crystals, as well as the crack path, are of particular interest.

SUMMARY AND CONCLUSIONS

A selected glass composition from the $MgO\text{-}Al_2O_3\text{-}SiO_2$ system and its crystallization behavior was investigated to shed light into the microstructure-mechanical properties relationships for the resulting hard, transparent glass-ceramics. The hardness, indentation cracking resistance, and fracture toughness (SEPB) of four glass-ceramics with different crystallized volume fractions were analyzed and discussed in light of the properties of the parent glass.

An indentation size effect was observed for loads below 10 N in the glass and the TGCs. The parent glass has a hardness of 8.5 ± 0.8 GPa, whereas it ranged from 9 to 10 GPa for the four transparent glass-ceramics studied here.

The K_{Ic} values (SEPB) differ considerably from the values estimated from the indentation deformation and cracking characteristics, corroborating reports by other authors. The fracture toughness increased by approximately 80 % (from 0.6 to 1.1 $MPa.m^{1/2}$) from glass to glass-ceramics. This finding corroborates previous studies dealing with the fracture toughness determination for brittle materials (especially glasses) which concluded to the unsuitability of indentation cracking technique (ICT) measurements. The fine dispersion of nanometric crystals is responsible for this reinforcement. Interestingly, the toughness improvement is noteworthy during the first 20 min of heat-treatment at 900 ºC, with minor change during the subsequent 2 hours, probably because the crystalized volume fraction did not change significantly during the applied heat treatment.

ACKNOWLEDGEMENTS

The authors would like to thank the São Paulo State Research Foundation - FAPESP for the following grants: BEPE Grant 2014/03004-0 and FAPESP CEPID Process 2013/07793-6. This study was financed in part by the

Coordenação de Aperfeiçoamento de Pessoal de Nível Superior - Brasil (CAPES) - Finance Code 001.

Funding: This work was supported by the São Paulo State Research Foundation – FAPESP [BEPE Grant 2014/03004-0 and FAPESP CEPID Process 2013/07793-6]; and by the Coordenação de Aperfeiçoamento de Pessoal de Nível Superior - Brasil (CAPES) - Finance Code 001.

References

[1] L. L. Hench, Bioglass: 10 milestones from concept to commerce. Journal of Non-Crystalline Solids. 2015; 432:7.

[2] Corning Incorporated. Advantaged properties of ultra low expansion glass.https://www.corning.com/worldwide/en/products/advanced-optics/product-materials/semiconductor-laser-optic-components/ultra-low-expansion-glass.html#:~:text=Advantaged%20properties%20of%20ultra%20low,thermal%20hysteresis%2C%20and%20delayed%20elasticity. Acessed August 30th, 2021.

[3] E. D. Zanotto, A bright future for glass-ceramics. American Ceramic Society Bulletin. 2010; 89:8.

[4] V. M. Fokin, E. D. Zanotto, N. S. Yuritsyn, J. W. P. Schmelzer, Homogeneous crystal nucleation in silicate glasses: A 40 years perspective. Journal of Non-Crystalline Solids. 2006; 352:33.

[5] W. Höland, G. H. Beall, Glass Ceramic Technology. 2nd Edition ed: Wiley, 2012.

[6] S. M. Salman, S. N. Salama, E. A. Mahdy, Preparation of magnetic glass-ceramics by crystallization of ternary eutectic Li_2O-MgO-SiO_2 system reformed with some di-and trivalent oxides. Ceramics International. 2018; 44:8.

[7] S. R. S Sanghi, N. Ahlawat, A. Agarwal, Crystallization kinetics, optical and dielectric properties of $Li_2O{\cdot}CdO{\cdot}Bi_2O_3{\cdot}SiO_2$ glasses. Journal of Molecular Structure. 2015; 1098:11.

[8] M. F. Ashby, D. R. H. Jones, Engineering Materials 1: An Introduction to Properties, Applications and Design: Butterworth-Heinemann, 2011.

[9] T. M. Cleary, J. G. Couillard, T. S. Huten, A. Jain, B. E. Marcellus, M. J. Moore, Methods for producing ion exchanged glass and resulting apparatus. In: Office USPaT, editor. USA: CORNING INCORPORATED; 2016.

[10] S. Rodríguez-López, J. Wei, K. C. Laurentic, I. Mathias, V. M. Justo, F. C. Serbena, C. Baudín, J. Malzbender, M. J. Pascual, Mechanical properties of solid oxide fuel cell glass-ceramic sealants in the system BaO/SrO-MgO-B_2O_3-SiO_2. Journal of the European Ceramic Society. 2017;37:15.

[11] V. O. Soares, J. K. M. B. Daguano, C. B. Lombello, O. S. Bianchin, L. M. G. Gonçalves, E. D. Zanotto, New sintered wollastonite glass-ceramic for biomedical applications. Ceramics International. 2018;44:8.

[12] F. C. Serbena, I. Mathias, C. E. Foerster, E. D. Zanotto, Crystallization toughening of a model glass-ceramic. Acta Materialia. 2015; 86:13.

[13] H. Meng, H. Xie, L. Yang, B. Chen, Y. Chen, H. Zhang, C. Chen, Effects of multiple firings on mechanical properties and resin bonding of lithium disilicate glass-ceramic. Journal of the Mechanical Behavior of Biomedical Materials. 2018; 88:7.

[14] L. S. Gallo, F. Célarié, N. Audebrand, A. C. M. Rodrigues, E. D. Zanotto, T. Rouxel, In situ crystallization and elastic properties of transparent MgO-Al_2O_3-SiO_2 glass-ceramic. Journal of the American Ceramic Society. 2017;100:10.

[15] R. Kumar, A. R. Molla, A. Chakrabarti, A. Tarafder, Eu^{3+}-doped transparent potassium lanthanum silicate ($KLaSiO_4$) glass-ceramic nanocomposites: Synthesis, properties and application. Journal of the European Ceramic Society. 2018; 38:9.

[16] M. I. Budd, J. G. Darrant, Glass-ceramic armour. Intellectual Property Office, GB 2284655. UK: GEC Alsthom; 1995. p. 16.

[17] T. B. Cunha, J. P. Wu, O. Peitl, V. M. Fokin, E. D. Zanotto, L. Iannucci, A. R. Boccaccini, Mechanical Properties and Impact Resistance of a New Transparent Glass-Ceramic. Advanced Engineering Materials. 2007; 9:6.

[18] T. M. Gross, H. Liu, Y. Zhai, L. Huang, J. Wu, The impact of densification on indentation fracture toughness measurements. Journal of the American Ceramic Society. 2019; 00:1–10. SPECIAL ISSUE ARTICLE. DOI: 10.1111/jace.16793.

[19] T. Rouxel, S. Yoshida, The fracture toughness of inorganic glasses, J. Am. Ceram. Soc. 2017; 100 4374–4396.

[20] V. M. Fokin, E. D. Zanotto, Surface and volume nucleation and growth in TiO2–cordierite glasses. Journal of Non-Crystalline Solids. 1999; 246:13.

[21] G. R. Anstis, P. Chantikul, B. R. Lawn, D. B. Marshall, A Critical Evaluation of Indentation Techniques for Measuring Fracture Toughness: I, Direct Crack Measurements. Journal of the American Ceramic Society. 1981; 64:6.

[22] Nose, T.; Fujii, T.; Evaluation of Fracture Toughness for Ceramic Materials by a Single-Edge-Precracked-Beam Method. Journal of the American Ceramic Society. 1988; 71:6.

[23] T. To, F. Célarié, C. Roux-Langlois, A. Bazin, Y. Gueguen, H. Orain, M. Le Fur, V. Burgaud, T. Rouxel, Fracture toughness, fracture energy and slow crack growth of glass as investigated by the Single-Edge Precracked Beam (SEPB) and Chevron-Notched Beam (CNB) methods, Acta Mater. 146 (2018) 1–11. doi:10.1016/j.actamat.2017.11.056.

[24] T. Nishida, T. Shiono, T. Nishikawa, On the Fracture Toughness of Polycrystalline Alumina Measured by SEPB Method. Journal of the European Ceramic Society. 1989; 5:5.

[26] H. Li, C. Bradt, The indentation load/size effect and the measurement of the hardness of vitreous silica. J. Non-Cryst. Solids 146, 197–212. (doi:10.1016/S0022-3093(05)80492-2)

[25] M. Kazembeyki, M. Bauchy, C. G. Hoover, New insights into the indentation size effect in silicate glasses. 2019 Journal of Non-Crystalline Solids, Volume 521. 9p

[26] L. S. Gallo, Vitrocerâmicas do sistema MgO – Al_2O_3 – SiO_2 para uso em proteção balística. Brazil: Universidade Federal de São Carlos, 2012.

[27] K. T. Faber, A. G. Evans, Crack deflection processes - I. Theory. Acta Metallurgica. 1983; 31:11.

[28] O. Peitl, E. D. Zanotto, F. C. Serbena, L. L. Hench, Compositional and microstructural design of highly bioactive P_2O_5–Na_2O–CaO–SiO_2 glass-ceramics, Acta Biomaterialia 8 (2012) 321–332.

FIGURES LEGENDS

Figure 1: Schematic of the bridge indentation technique. The sample is inserted between two SiC bars, the lower one having a groove of 3.4 mm to induce tensile stress at the bottom of the sample [22].

Figure 2: DSC traces of the studied composition. Adapted from [14].

Figure 3: Vickers indent performed on parent glass samples. a) 600 mN; b) 1 N; c) 4.9 N; d) 9.8 N; e) 49.03 N; f) 98.07 N and g) 196.1 N.

Figure 4: Vickers hardness as a function of the applied load for the glass sample of the composition shown in Table 1. The range of ISE (Indention Size Effect) is shown.

Figure 5: Indent profile for different applied loads in the investigated MAS glass-ceramics obtained for the same nucleation treatment (48h at 733 ºC) and crystal growth treatments at 900 ºC for: a) 31 min; b) 61 min; c) 92 min d) 153 min. The scale is the same for all images obtained under the same load.

Figure 6: a) Hardness for different loads for glass-ceramic samples and b) hardness versus crystal growth time at 900 ºC, after 48 h at 733 ºC, for different loads. Error bars represent the standard deviation of at least five imprints.

Figure 7: Example of the fracture surface of a glass-ceramic specimen after the 3-point bending fracture stage. The pre-crack region is clearly visible at the bottom, as well as the pre-crack arrest line standing as the frontier to the fast crack extension region (upper region). The glass-ceramic was obtained after heat treatment for 48 h at 1006 K and 153 min at 900 °C.

Figure 8: K_{IC} values obtained by Single Edge Pre-cracked Beam (SEPB) and indentation cracking (ICT) resistance using the Anstis equation (19), for the precursor glass and glass-ceramics obtained after different crystal growth periods at 900 ºC.

Figure 9: STEM-images in bright and dark field modes of glass-ceramics obtained after nucleation treatment at 48h at 733 ºC and growth treatment of a) 31 min at 900 ºC; b) 61 min at 900 ºC; c) 92 min at 900 ºC and d) 153 min at 900 ºC.

Figure 10: Evolution of Mg distribution in the glass-ceramics obtained after a nucleation step of 48h at 733 ºC and a growth treatment at 900 ºC for: a) 31 min. b) 61 min c) 92 min. d) 153 min.

Figure 11: The evolution of Ti distribution in glass-ceramics obtained after a nucleation step of 48h at 733 ºC and a growth treatment at 900 ºC for: a) 31 min. b) 61 min c) 92 min. d) 153 min.

Figure 12: Evolution of Al distribution in the glass-ceramics obtained after a nucleation step of 48h at 733 ºC and a growth treatment at 900 ºC for: a) 31 min. b) 61 min c) 92 min. d) 153 min.

TABLE

Table 1: Molar and weight % composition of the investigated glass.

Oxide	mol%	mass%
Al_2O_3	17.67	26.15
SiO_2	55.52	48.41
B_2O_3	1.50	1.52
TiO_2	6.90	8.00
MgO	16.66	9.74
ZrO_2	0.50	0.89
Sb_2O_3	1.25	5.29

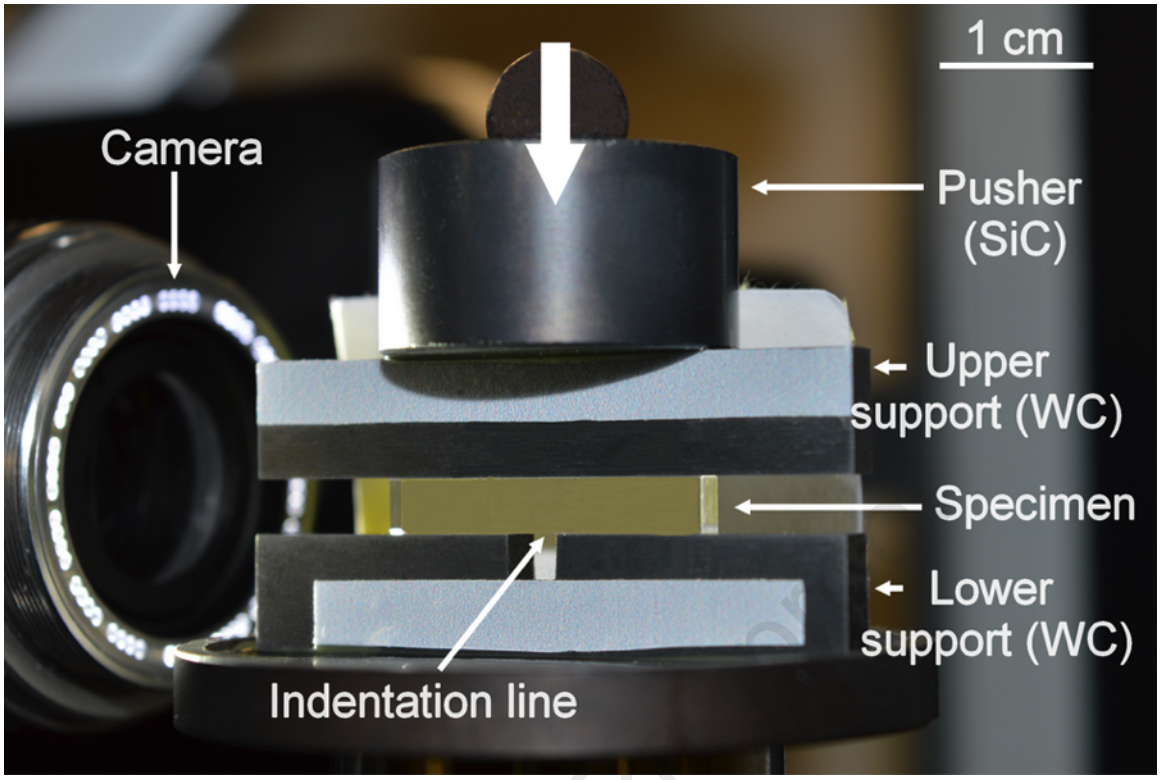

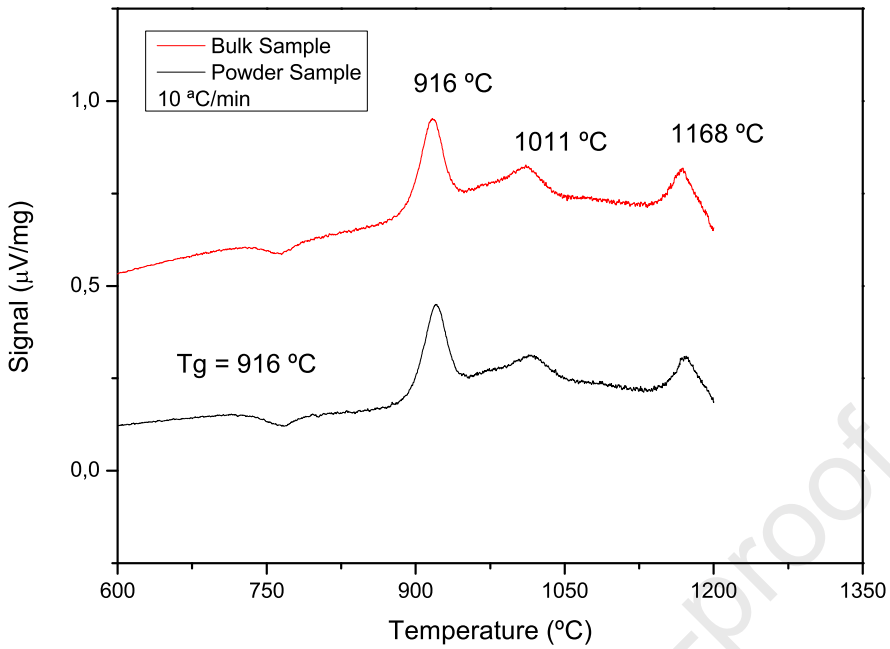

a) 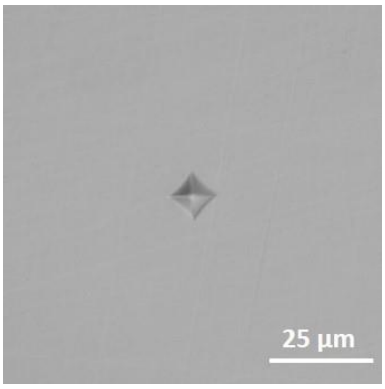

b) 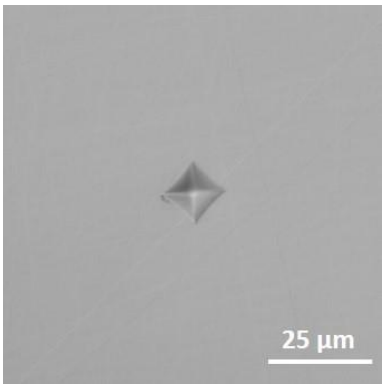

c) 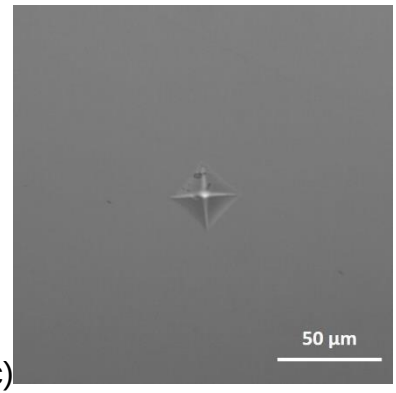

d) 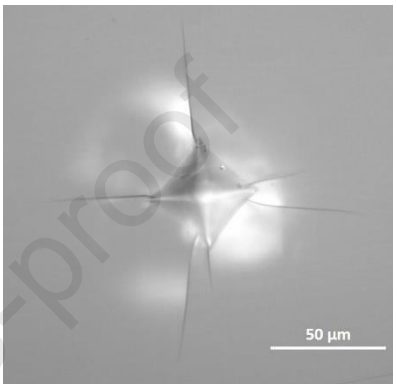

e) 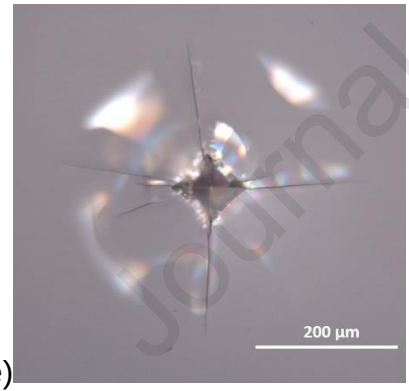

f) 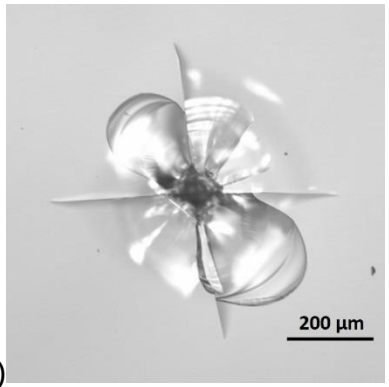

g) 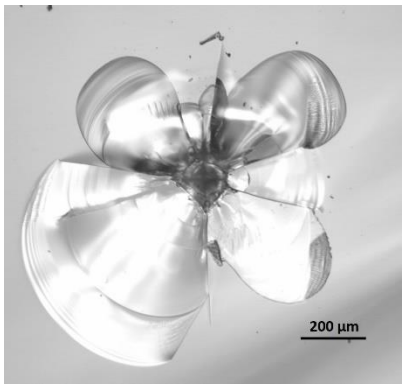

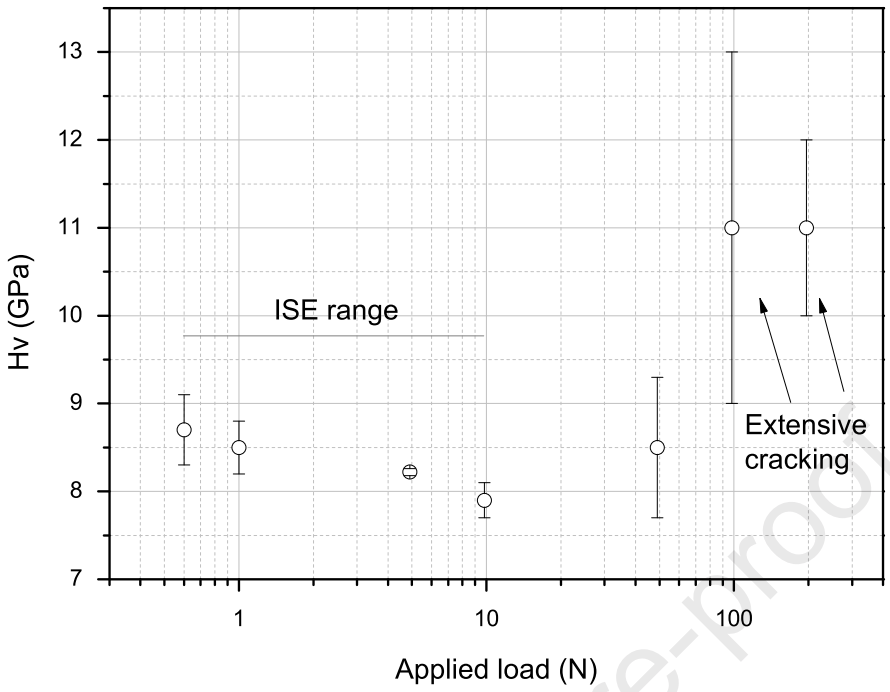

4.9 N

a) 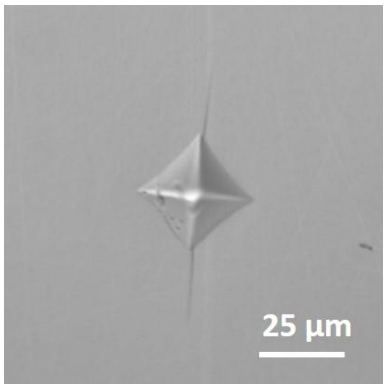

b) 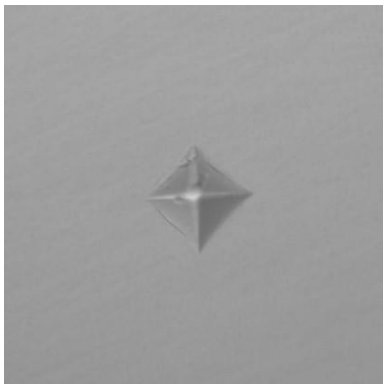

c) 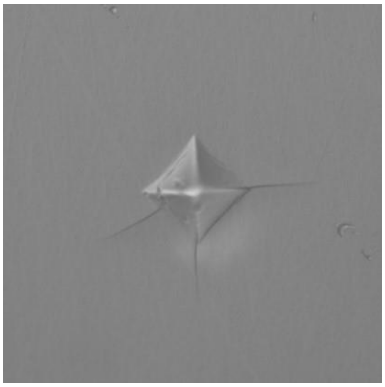

d) 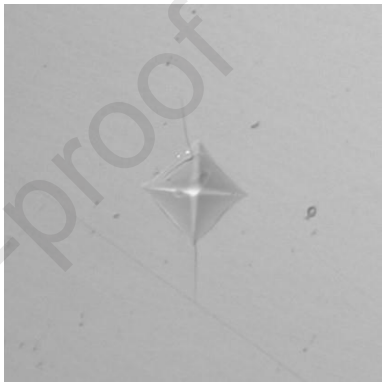

9.8 N

a) 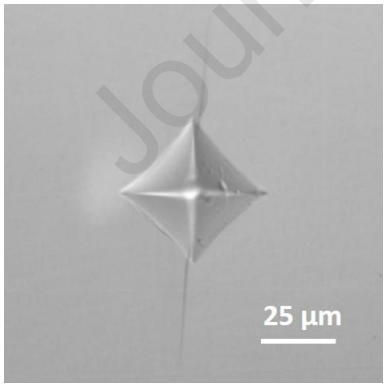

b) 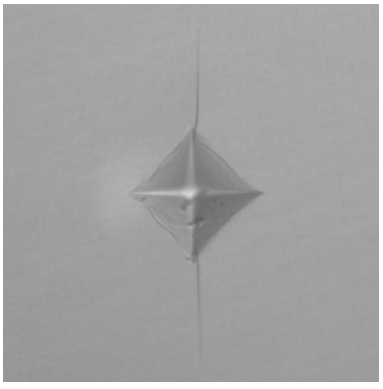

c) 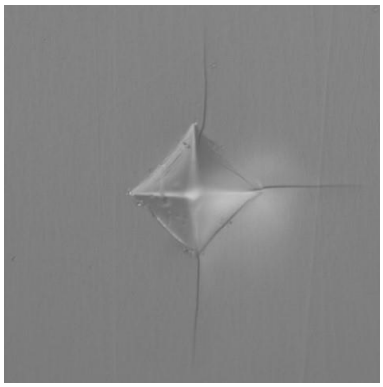

d) 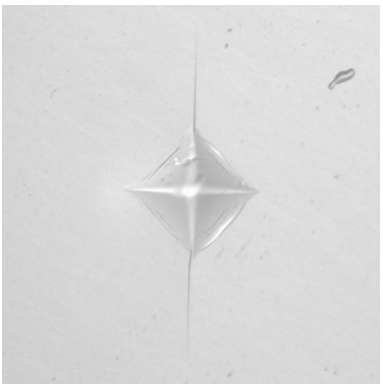

49.03 N

a) 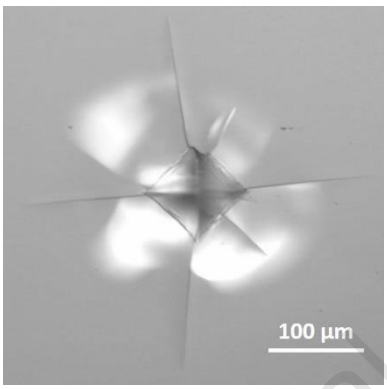

b) 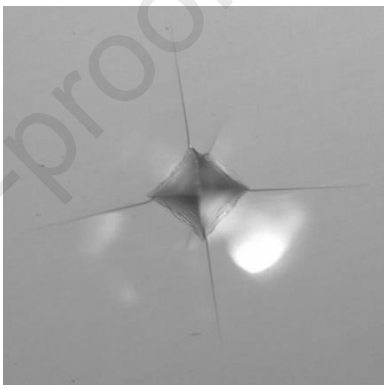

c) 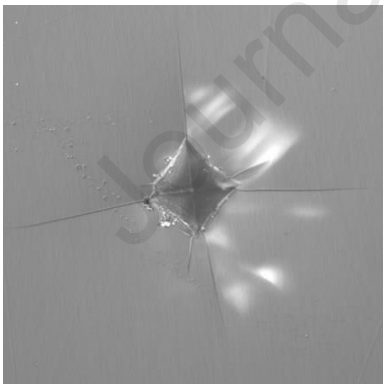

d) 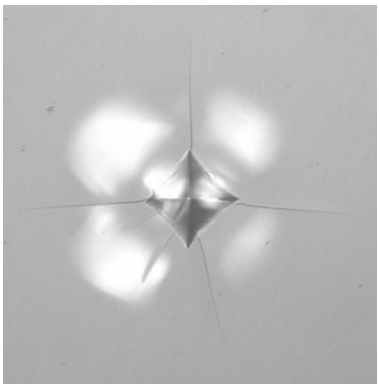

98.07 N

a) 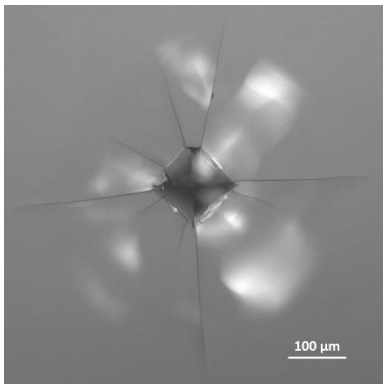

b) 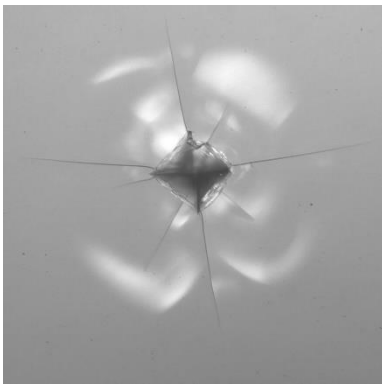

c) 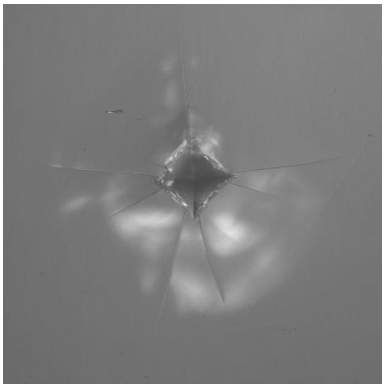

d) 

196.1 N

a) 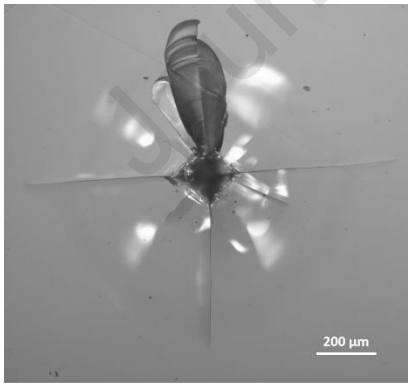

b) 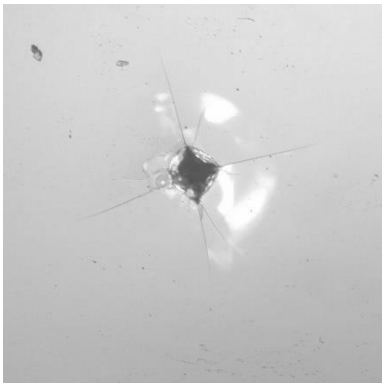

c) 

d) 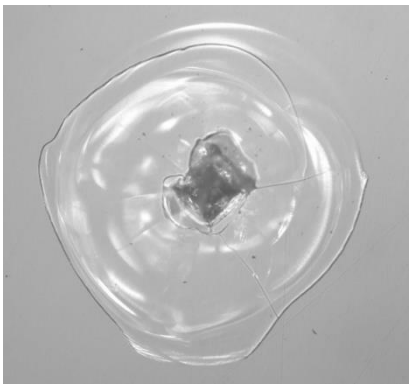

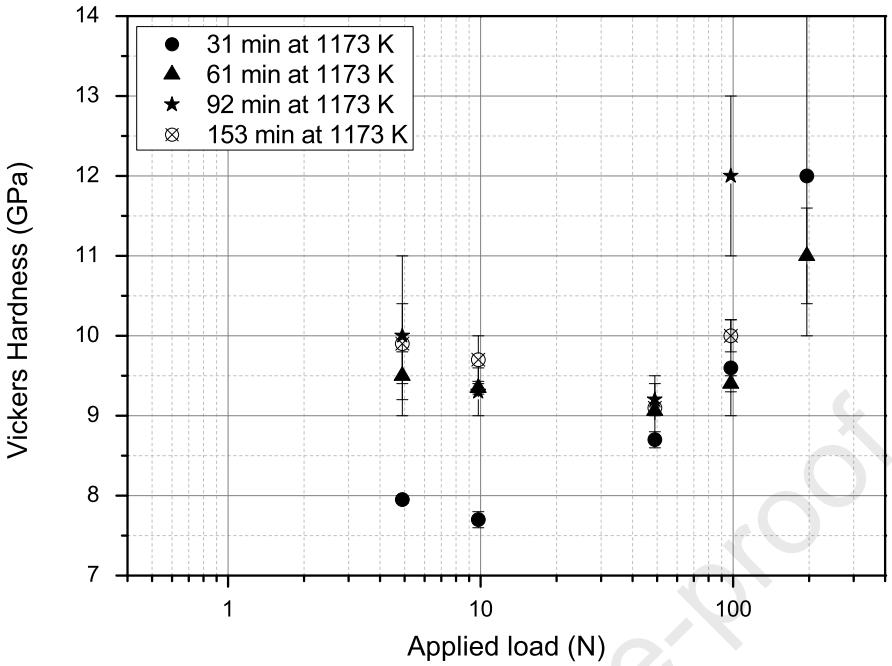

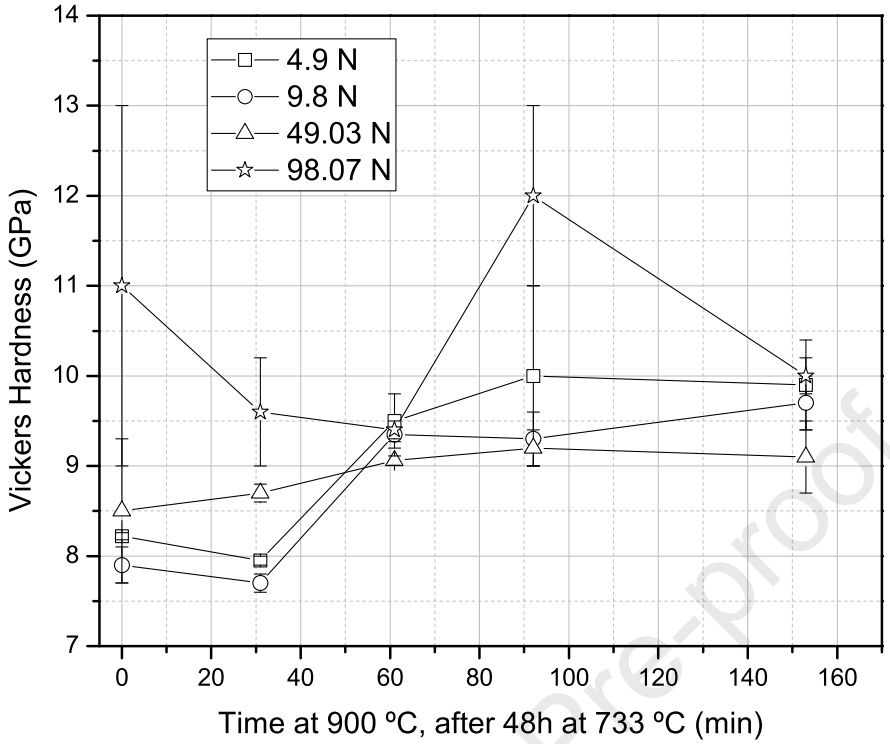

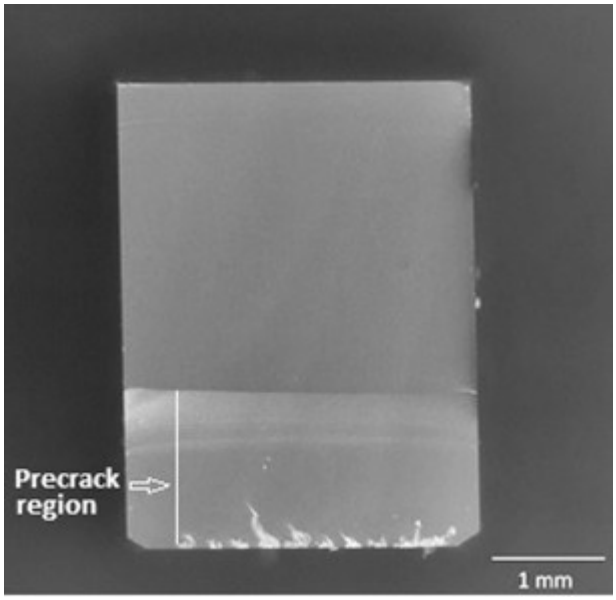

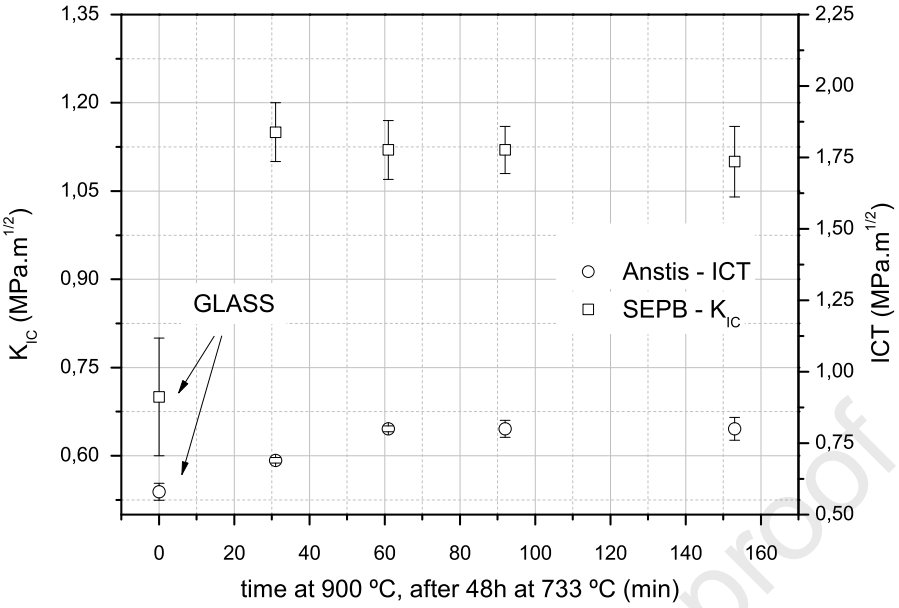

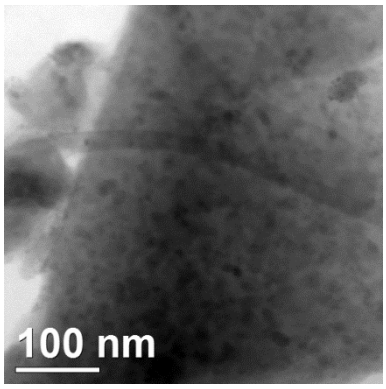

bright field

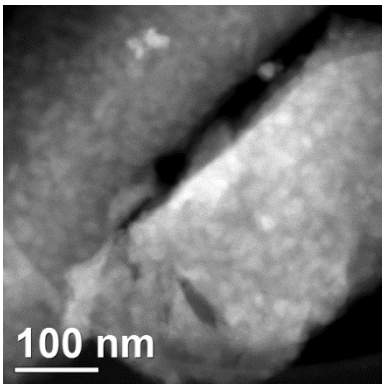

dark field

a)

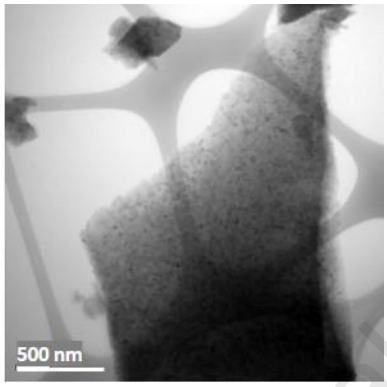

bright field

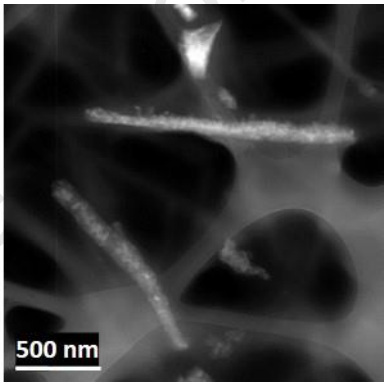

dark field

b)

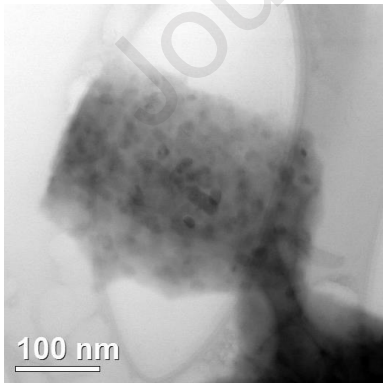

bright field

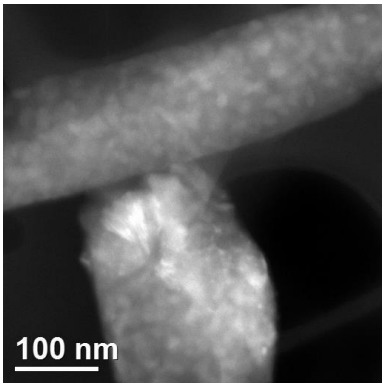

dark field

c)

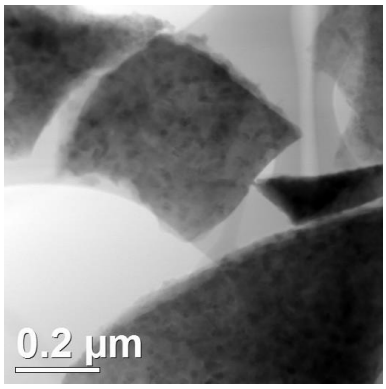

bright field

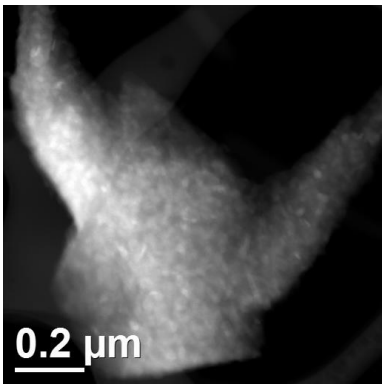

dark field

d)

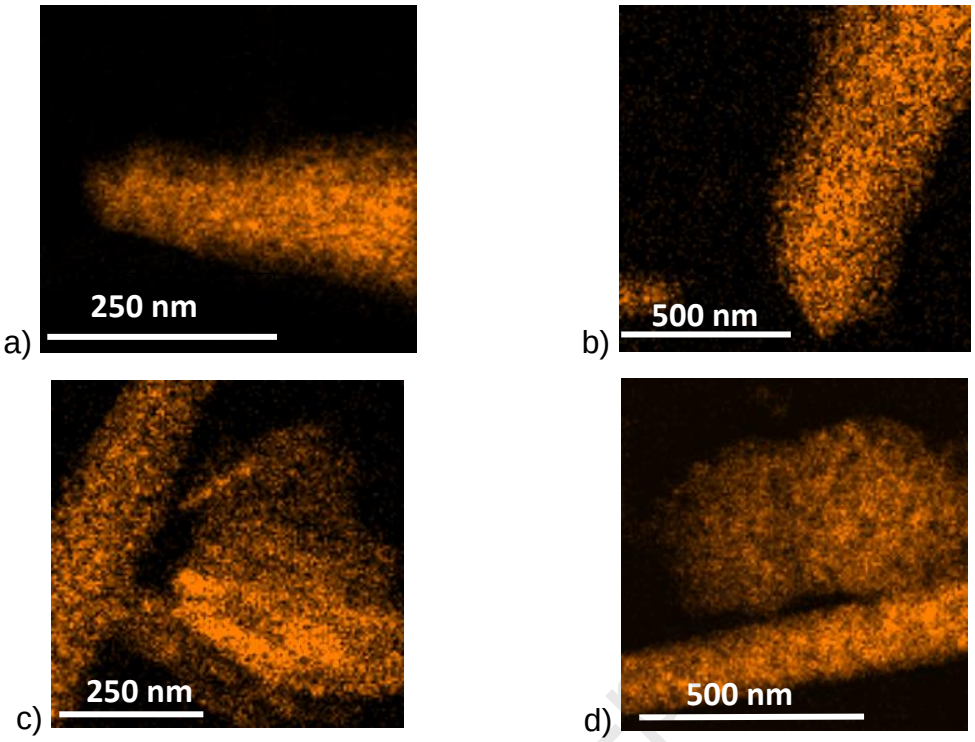

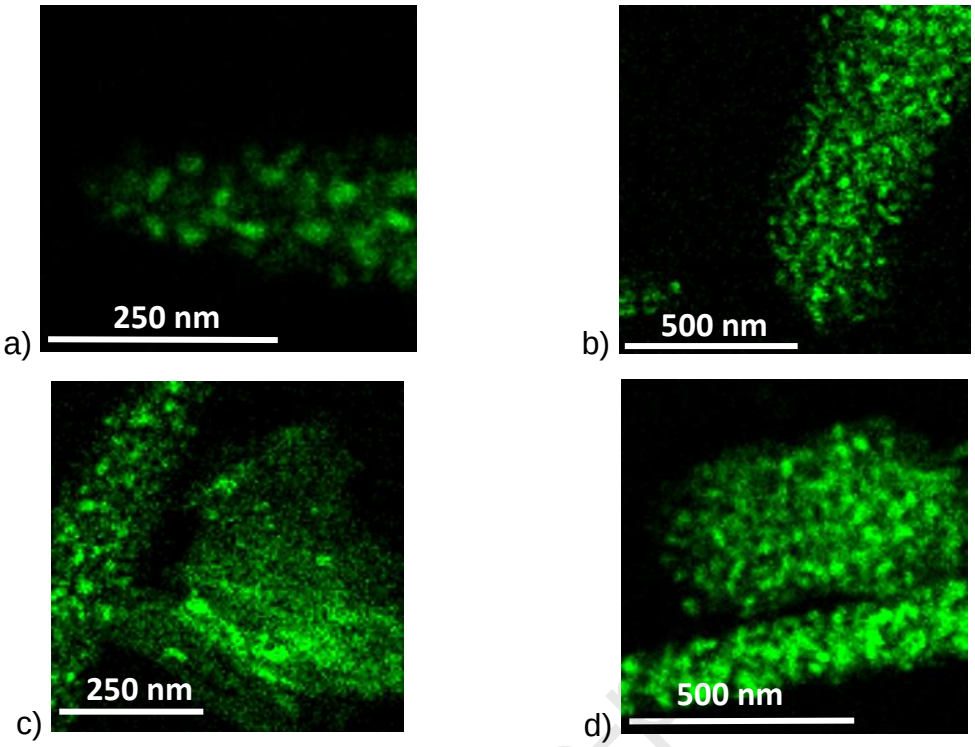

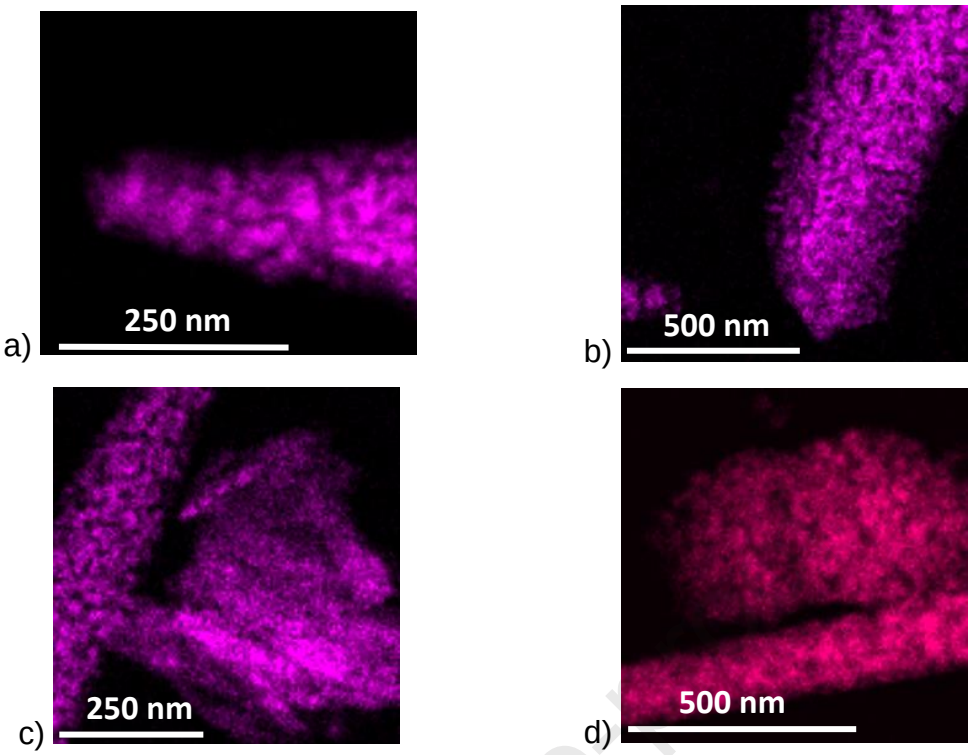

Declaration of interests

☒ The authors declare that they have no known competing financial interests or personal relationships that could have appeared to influence the work reported in this paper.

☐The authors declare the following financial interests/personal relationships which may be considered as potential competing interests: